Electronic Supplementary Information

Pt^{2+}-exchanged ZIF-8 nanocube as a solid-state precursor for $L1_0$-PtZn intermetallic nanoparticles embedded in a hollow carbon nanocage

Taehyun Kwon,[a,†] Sunghyun Lim, [a,†] Minki Jun, [a] Minjung Kang, [a] Jinwhan Joo, [a] Aram Oh, [b] Hionsuck Baik, [b] Chang Seop Hong [a] and Kwnagyeol Lee [a,*]

[a.] Department of Chemistry and Research Institute for Natural Sciences, Korea University, Seoul 02841, Republic of Korea. E-mail: kylee1@korea.ac.kr

[b.] Seoul Center, Korea Basic Science Institute (KBSI), Seoul 02841, Republic of Korea.

[†]These authors contributed equally to this work.

Additional Experimental Details

Synthesis of ZIF-8 rhombic dodecahedra (RD).

The synthetic procedure was adopted and slightly modified from the previously reported literature.[S1] In a typical synthesis, $Zn(NO_3)\cdot 6H_2O$ (3.1 mmol, 0.59 g) was dissolved in 15 mL MeOH. In another vessel, 2-MeIm (7.55 mmol, 0.62 g) was dissolved in 15 mL MeOH. The above mentioned two solutions are mixed and kept under 35 ^oC for 12 h without stirring. The product could be obtained by centrifuging with added methanol.

Preparation of carbon-supported EZPC-X (EZPC-X/C) catalyst.

Carbon-supported EZPC-X (EZPC-X/C) were prepared by supporting EZPC-X particles on carbon support. The EZPC-X was dispersed in ethanol and the slurry was sonicated by ultrasonic processor (VC-505) for 30 min. In a separate vessel, carbon black (Vulcan XC-72, Cabot) was dispersed in ethanol and sonicated for 30 min. The slurry containing EZPC-X was added dropwise to the carbon-containing slurry and the mixture was sonicated further for 30 min. The black precipitate was obtained by centrifuging and washing several times with ethanol and dried overnight under vacuum condition.

Materials characterization.

Scanning electron microscopy (SEM) was performed on a Hitachi S-4700 filed emission SEM operating at 15 kV. Transmission electron microscopy (TEM) was performed on a TECNAI G2 20 S-Twin operated at 200 kV and a TECNAI G2 F30ST operated at 300 kV. Scanning TEM (STEM), high-resolution STEM (HR-STEM) energy dispersive X-ray spectroscopy (EDX) and aberration-corrected imaging and high-spatial-resolution EDX analyses were carried out on a FEI Titan Cubed 60-300 with Chemi-STEM technology and JEOL ARM200F Cs STEM. Powder X-ray diffraction (PXRD) patterns were collected with a Rigaku Ultima III diffractometer system

using a graphite-monochromatized Cu-Kα radiation at 40 kV and 30 mA. X-ray photoelectron spectroscopy (XPS) analysis was conducted with ULVAC-PHI X-tool X-ray photoelectron spectrometer. The source was monochromatic Al-Kα radiation (1486.6 eV) at 24.1 W. The carbon (C 1s) line at 284.6 eV was used as the reference line. X-ray absorption spectroscopy (XAS) including X-ray absorption near edge structure (XANES) analyses of Zn K-edge and Pt L_3-edge were conducted by using the beamline 7D of Pohang Accelerator Laboratory (PAL) in Republic of Korea. The monochromatized X-ray from a double crystal monochromator with Si(111) crystals was used for the energy scan. The XANES spectra were obtained at room temperature in transmission mode using an Ar/He ionization detector. The XANES spectra were calibrated by the reference metal foils; Zn K-edge and Pt L_3-edge for 9659 and 11564 eV, respectively. IR spectra were obtained with an ATR module using a Nicolet iS10 FT-IR spectrometer. Thermogravimetric analyses (TGA) were carried out under a N_2 (99.999%) atmosphere (flow rate = 40 mL min^{-1}) in the temperature range 25 – 900 ^oC (heating rate = 10 ^oC min^{-1}) using a Scinco TGA-N 1000 instrument. Metal (Pt, Zn) contents in the samples were analyzed using inductively coupled plasma atomic emission spectroscopy (ICP-AES) analyzer (700-ES, Varian).

Gas sorption measurement.

Gas sorption isotherms were measured using a BEL Belsorp mini II gas adsorption instrument up to 1 atom of gas pressure. The desolvated samples (EZP-Xs) were prepared under vacuum ($<10^{-3}$ torr) at room temperature for 12 hours. The isotherms were measured at 77 K using highly pure N_2 (99.999%).

Electrochemical characterization.

Electrochemical measurements were conducted with an electrochemical workstation (CHI7007E, CH Instruments) and a rotator (RRDE-3A, ALS) at room temperature. A three-

electrode system was built glassy carbon (GC) disk electrode, Ag/AgCl (filled with saturated KCl), and graphite rod as working, reference and counter electrodes, respectively. All data are given after conversion to the reversible hydrogen electrode (RHE) scale by measuring the open circuit potential of Ag/AgCl electrode with RHE ($H^+|H_2$ equilibrium on the Pt electrode).

Preparation of working electrode.

The GC disk electrode (5 mm in diameter) was polished on a micro-cloth with a 1 μm diamond suspension and 0.05 μm alumina suspension before using. Catalyst ink was composed of the catalyst, deionized water, 5 wt% Nafion (catalyst:Nafion mass ratio of 5:1) and isopropanol, which was ultrasonicated at least 30 min (0.6 mg_{Pt} mL^{-1}). 10 wt% Pt/C catalyst (Alfa Aesar) was used as a benchmark catalyst for comparison. 4.5 μL of the ink was dropped onto the GC disk and spun at 700 rpm for 2 min. Thereafter, the electrode was placed in an oven at 60 °C at least 5 min until completely dry. The catalyst loading on the electrode was controlled to be 14 μg_{Pt} cm^{-2}. The GC electrode with the catalyst film was equipped on a rotation shaft for electrochemical measurements.

Electrochemical active surface area (ECSA) measurement.

Electrochemical cleaning was conducted by cyclic voltammetry (CV) in the potential range of 0.05 – 1.2 V (vs. RHE) at a scan rate of 500 mV s^{-1} for 100 cycles in N_2-saturated 0.1 M $HClO_4$. The CV curves were obtained under the same conditions above, except that the scan rate was changed to 50 mV s^{-1} for 3 cycles. The electrochemical active surface areas (ECSAs) were estimated using the hydrogen underpotential deposition (H_{upd}) and the CO-stripping method. Measurements with H_{upd} were performed by saturating the electrolyte with N_2 gas before collecting the CV at a sweep rate of 50 mV s^{-1}. The H_{upd}-derived ECSA (ECSA-H_{upd}) was estimated by integrated charge from H_{upd} peak, which is observed between 0.05 and 0.35 V (vs. RHE). CO-

stripping measurements were performed by bubbling CO (20%, Ar-balanced) for 5 min through the 0.1 M $HClO_4$ while holding the potential at 0.15 V (vs. RHE). N_2 was then subsequently bubbled for 10 min to remove CO from the electrolyte, and three CV scans were then performed in the potential range of 0.05 – 1.2 V (vs. RHE) at a scan rate of 50 mV s^{-1} to completely desorb CO. The CO-stripping current density was measured by the first CV scan, and background current density was measured by the third CV scan after the complete desorption of CO. The CO-stripping peaks was obtained by subtraction of the third CV scan from the first CV scan. The CO-stripping-derived ECSA (ECSA-CO) of the catalysts were also estimated by integrating charge from CO-stripping peak observed above 0.6 V (vs. RHE).

Electrochemical methanol oxidation reaction (MOR).

The MOR activities of catalysts were evaluated from CV curves using a potential cycle from 0.05 to 1.2 V (vs. RHE) in N_2-saturated 0.1 M $HClO_4$ + 1.0 M MeOH solution at a rotation speed of 2,500 rpm and scan rate of 50 mV s^{-1}. Long-term durability of the catalysts was conducted in N_2-saturated 0.1 M $HClO_4$ + 1.0 M CH_3OH solution in a potential range from 0.4 to 0.9 V (vs. RHE) at a scan rate of 100 mV s^{-1} for 1000 cycles. After the cycling, the MOR activity was measured in fresh electrolyte. The MOR CVs before and after potential cycling were obtained under the same conditions as the ones used for the above MOR measurement. Chronoamperometry (CA) curves of the catalysts were recorded for 1000 seconds in N_2-saturated 0.1 M $HClO_4$ + 1.0 M MeOH solution at 0.9 V (vs. RHE). Electrochemical impedance spectra (EIS) were obtained at 0.60 V (vs. RHE) with AC potential amplitude of 10 mV from 10000 to 1 Hz in an N_2-saturated 0.1 M $HClO_4$ + 1.0 M MeOH solution with N_2 purging at a rotation speed of 2500 rpm.

Supporting Tables S1 and S2

Table S1. ICP-AES results of ZIF-8 NC and EZP-X (X = LL, L, M and H) nanoparticles.

	Zn		Pt	
	Weight %	**Atomic %**	**Weight %**	**Atomic %**
ZIF-8 NC	25.1	100	-	
EZP-LL	25.3	92.0	6.6	8.0
EZP-L	27.4	85.1	14.3	14.9
EZP-M	13.7	53.1	36.1	46.9
EZP-H	7.7	29.9	53.8	70.1

Table S2. ICP-AES results of EZPC-X/C (X = LL, L, M and H).

	Zn		Pt	
	Weight %	**Atomic %**	**Weight %**	**Atomic %**
EZPC-LL/C	3.2	73.7	3.4	26.3
EZPC-L/C	7.3	62.8	12.9	37.2
EZPC-M/C	3.5	45.1	12.7	54.9
EZPC-H/C	1.3	34.4	7.4	65.6

Supporting Figs. S1 to S33

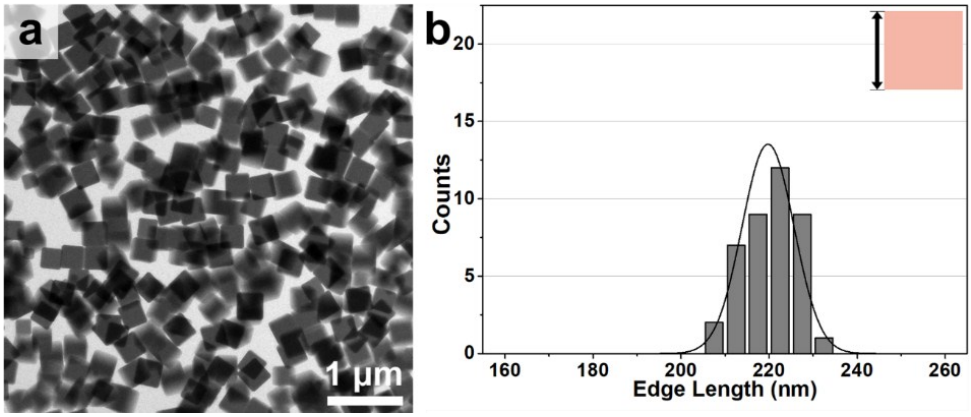

Fig. S1. Characterization of ZIF-8 nanocubes (ZIF-8 NCs). (a) Low magnification TEM image of ZIF-8 NCs. (b) Edge length distribution histogram of ZIF-8 NCs.

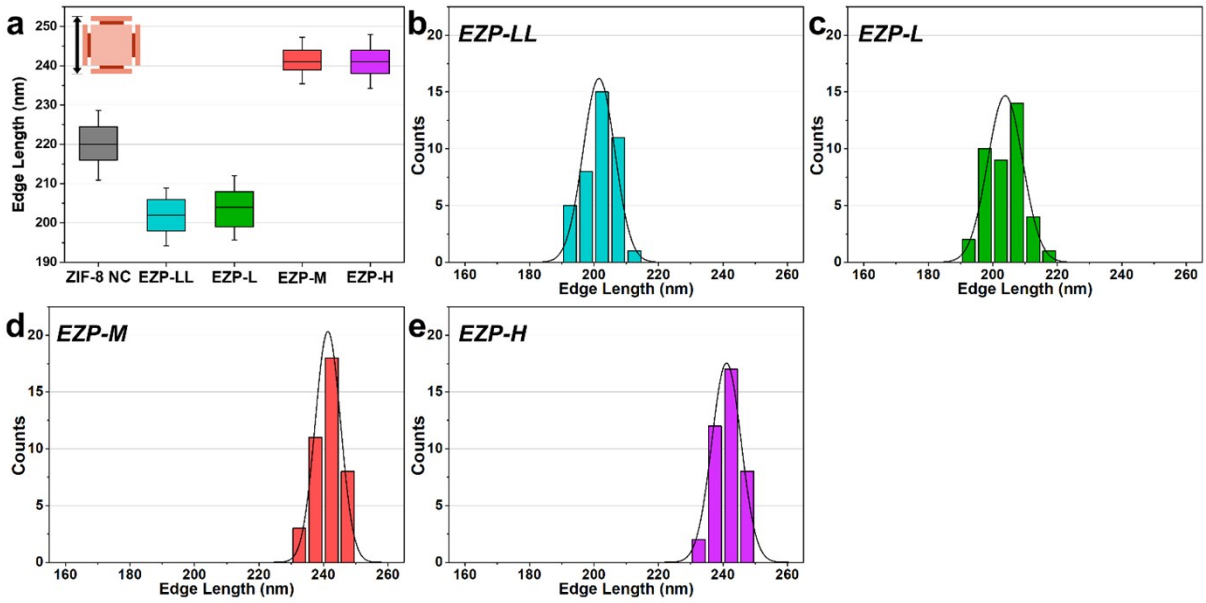

Fig. S2. (a) Edge length distribution of ZIF-8 NCs and edge-etched ZIF-8/Pt nanocubes (EZP-X). (b-e) Edge length distribution histogram of (b) EZP-LL, (c) EZP-L, (d) EZP-M and (e) EZP-H.

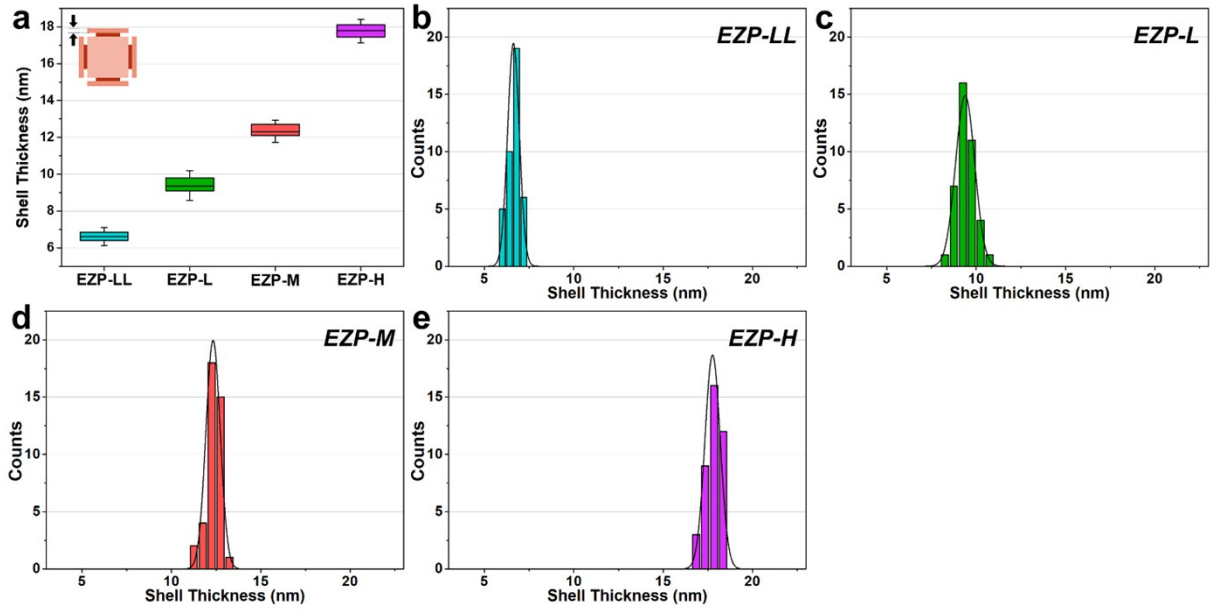

Fig. S3. (a) Shell thickness distribution of EZP-X. (b-e) Shell thickness histogram of (b) EZP-LL, (c) EZP-L, (d) EZP-M and (e) EZP-H.

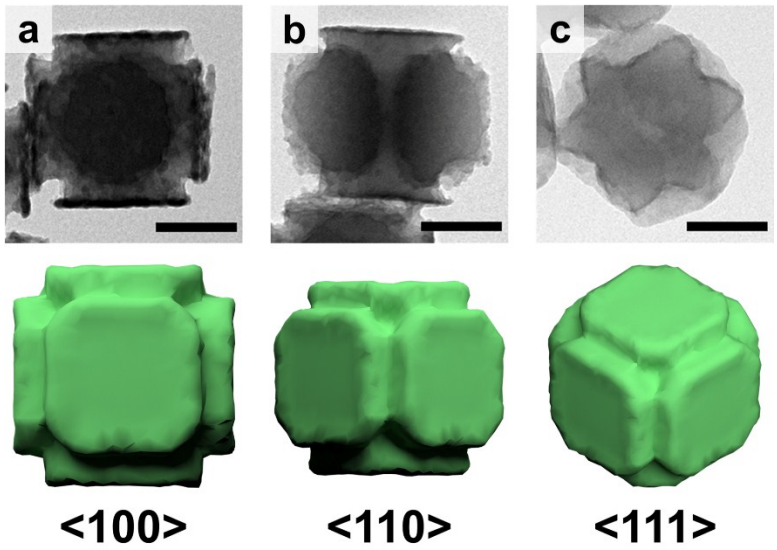

Fig. S4. TEM images and corresponding structural models of EZP-L viewed from different zone axes. (a) <100>, (b) <110> and (c) <111>. Scale bar = 100 nm.

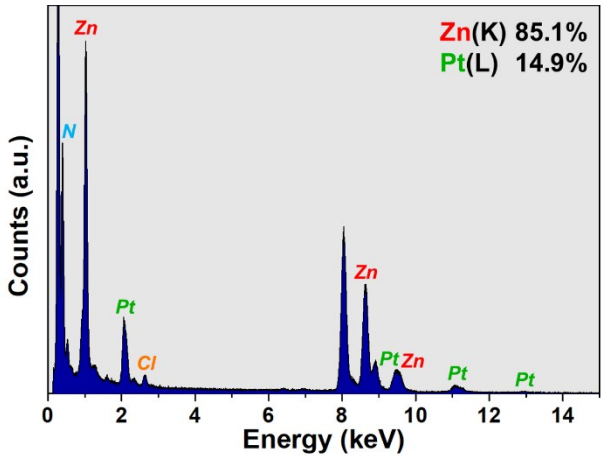

Fig. S5. EDX spectrum of EZP-L. N content from 2-MeIm ligand and Cl content are also observed. Samples were prepared on Cu TEM grid.

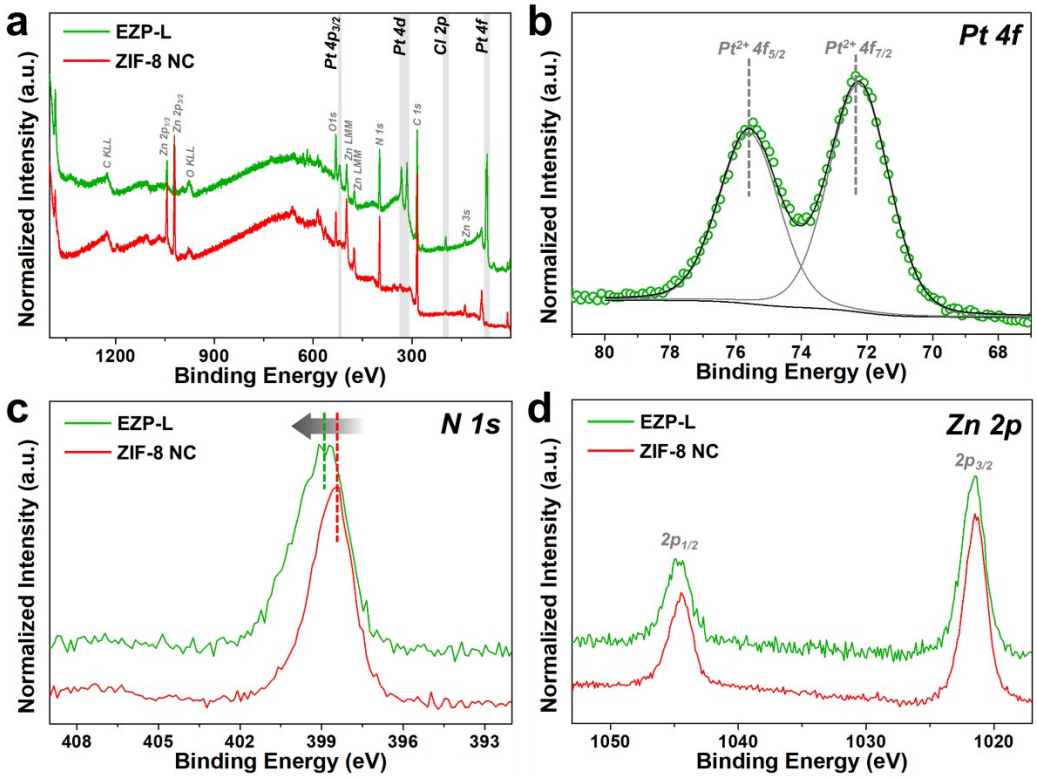

Fig. S6. XPS analyses of EZP-L and ZIF-8 NC. (a) XPS survey spectra of EZP-L and ZIF-8 NC. (b) Pt 4f XPS spectrum of EZP-L. (c) N 1s XPS spectra of EZP-L and ZIF-8 NC. (d) Zn 2p XPS spectra of EZP-L and ZIF-8 NC.

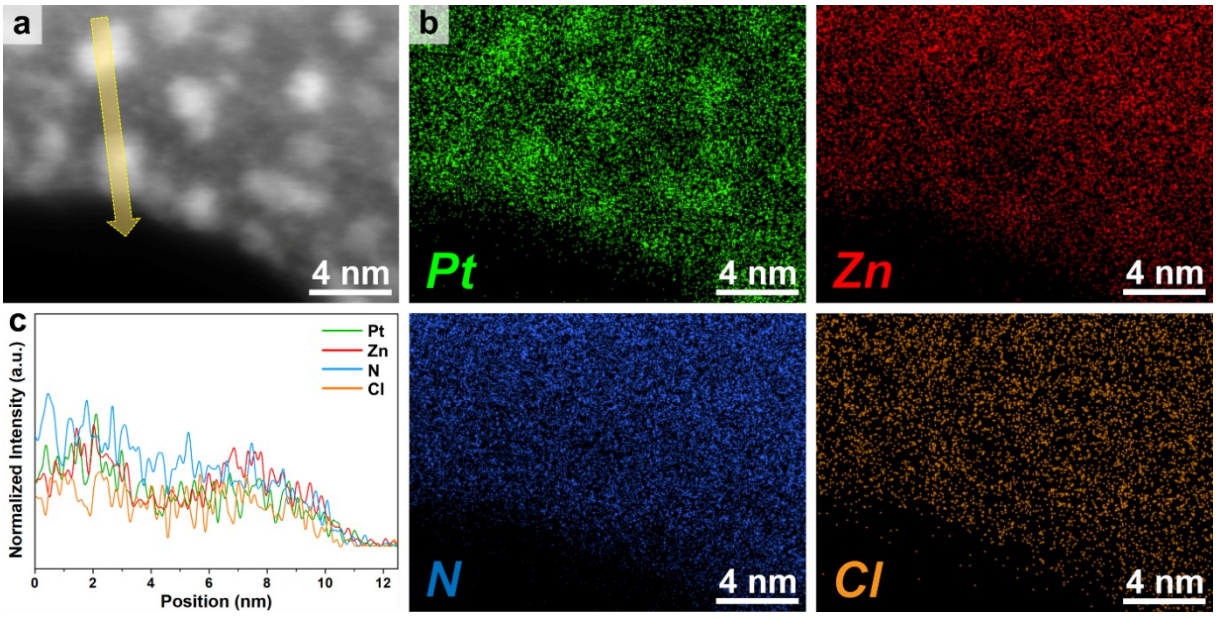

Fig. S7. Analysis of the outer shell of EZP-L. (a) Enlarged HAADF-STEM image of the outer shell of EZP-L. (b-c) Corresponding EDX (b) elemental mapping and (c) line profile analysis of Pt (green), Zn (red), N (blue) and Cl (orange) content in the edge of EZP-L, shown in Fig. S7a.

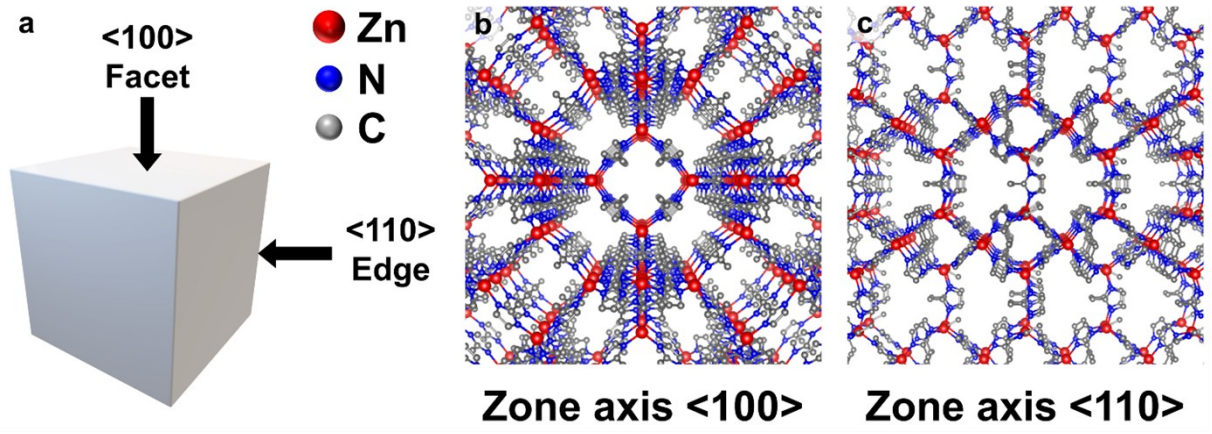

Figure S8. Structural modelling of ZIF-8 NCs. (a) Schematic illustration of nanocube structure and the relations of its facet, edge to the crystallographic directions of cubic structure. (b-c) Atomic orientations of ZIF-8 crystals (b) from the facet (zone axis <100> direction), and (c) from the edge (zone axis <110> direction). Hydrogen atoms are omitted for clarity.

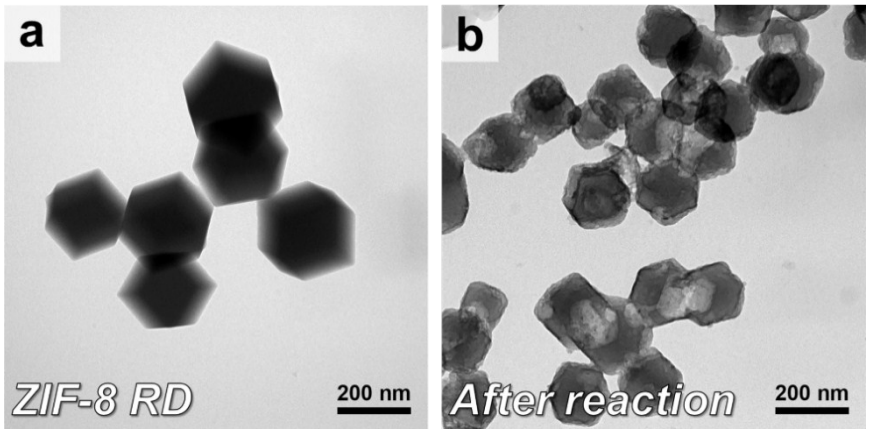

Figure S9. TEM images of ZIF-8 rhombic dodecahedra (RD) (a) before and (b) after reaction with K_2PtCl_4 precursor.

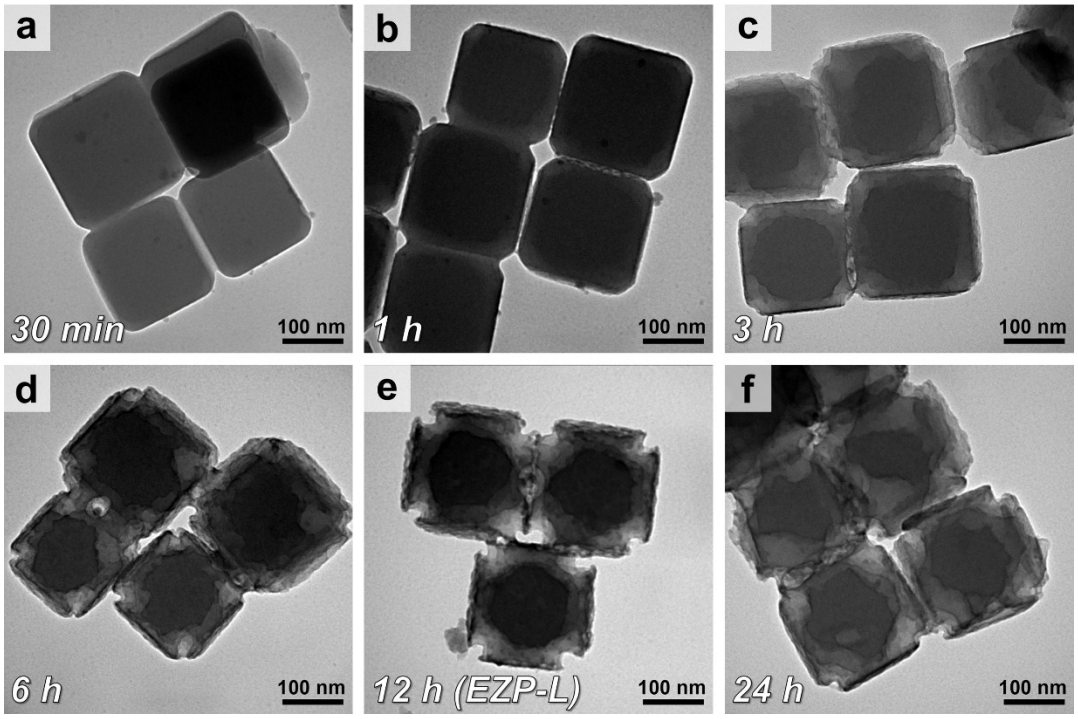

Figure S10. TEM images of reaction intermediates of EZP-L from 30 min to 24 h: (a) 30 min, (b) 1 h, (c) 3 h, (d) 6 h, (e) 12 h (EZP-L) and (f) 24 h after reaction.

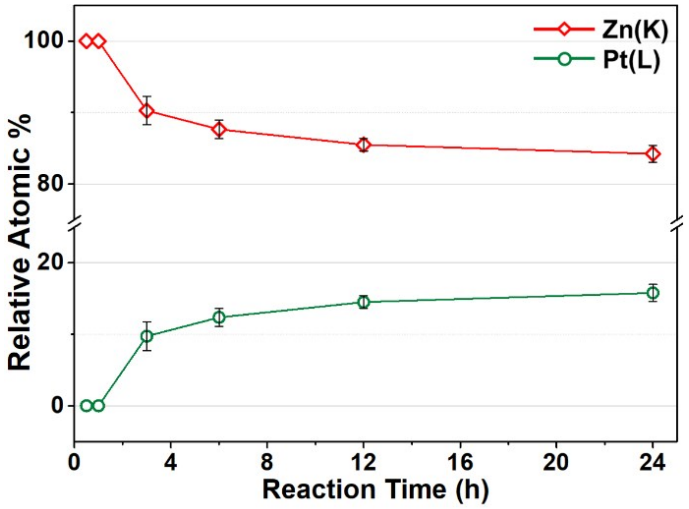

Figure S11. Relative atomic percent change in Zn and Pt contents of reaction intermediates of EZP-L measured by EDX. The measurement was conducted at least 3 times and the samples were prepared on Cu TEM grids.

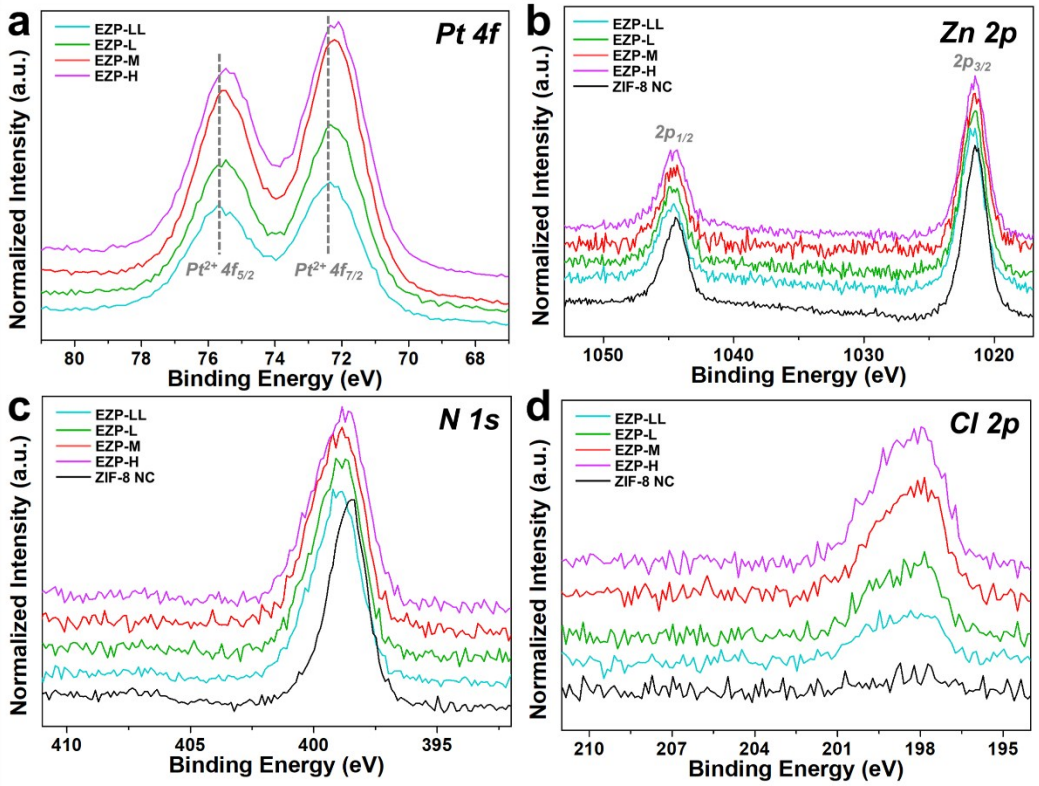

Figure S12. XPS analyses of EZP-LL, EZP-L, EZP-M, EZP-H and ZIF-8 NC: (a) Pt 4f, (b) Zn 2p, (c) N 1s and (d) Cl 2p spectra.

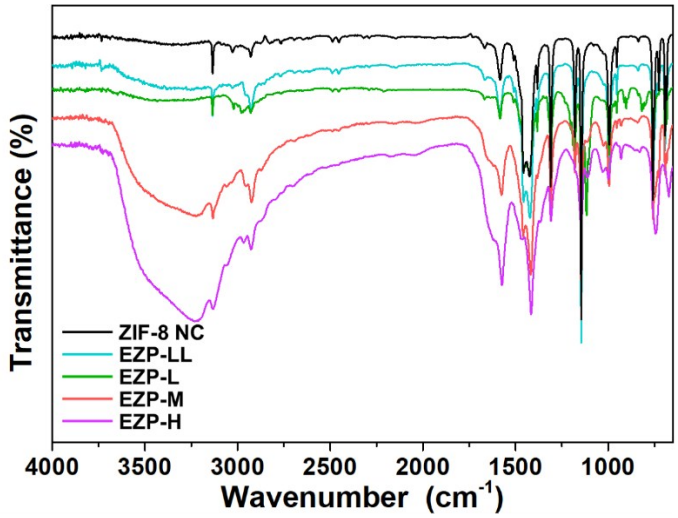

Figure S13. FTIR spectra of ZIF-8 NC, EZP-LL, EZP-L, EZP-M and EZP-H.

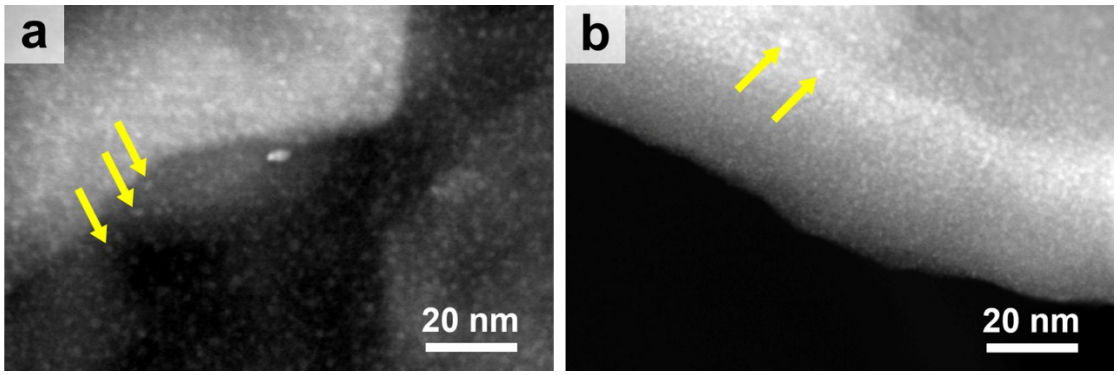

Figure S14. HAADF-STEM images of the outer shell of (a) EZP-M and (b) EZP-H. Yellow arrows in the HAADF-STEM images indicate the Pt^{2+}-rich aggregates whose sizes are under 5 nm.

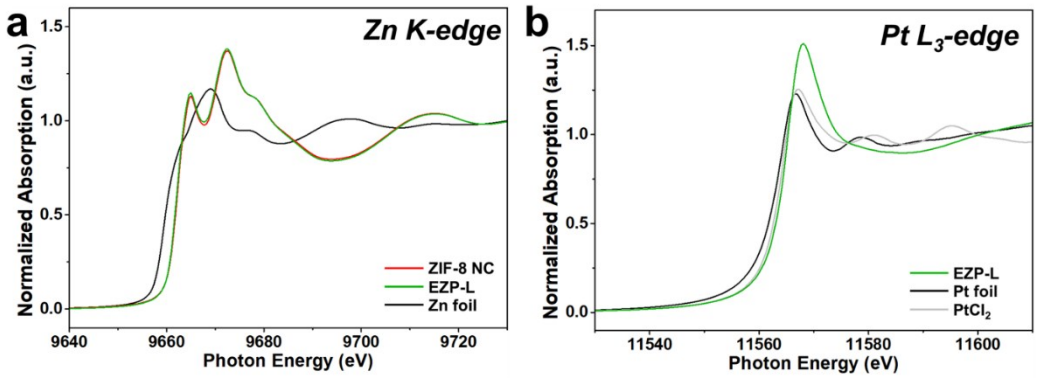

Figure S15. (a) Zn K-edge XANES spectra of ZIF-8 NC, EZP-L and Zn foil. (b) Pt L_3-edge XANES spectra of EZP-L, Pt foil and $PtCl_2$.

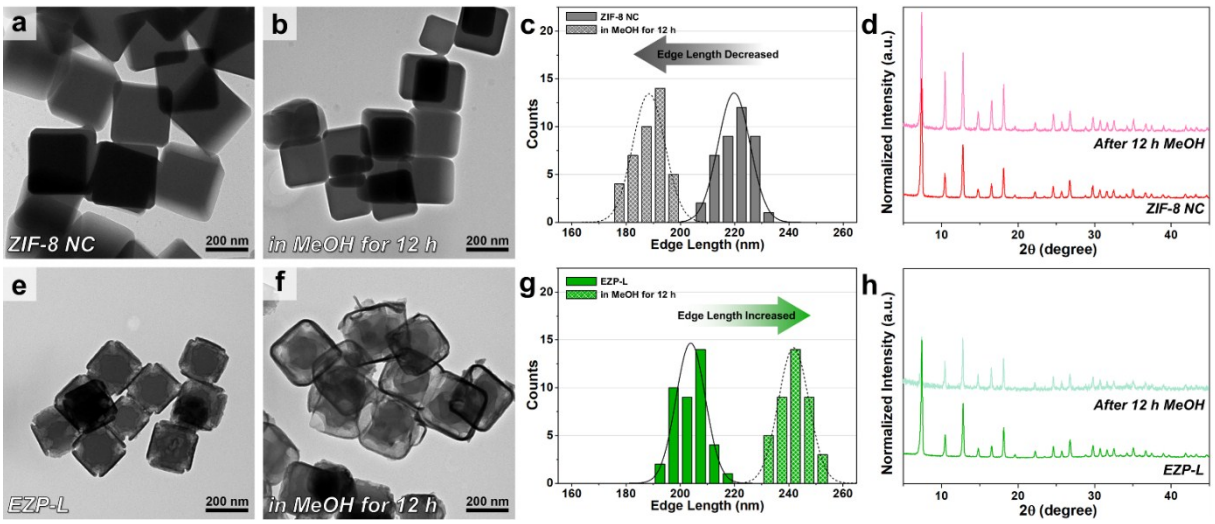

Figure S16. Phase stability of ZIF-8 crystal structure in ZIF-8 NCs and EZP-L. (a, b) TEM images of (a) pristine ZIF-8 NCs and (b) soaked in MeOH for 12 h. (c) Edge length distribution histogram and (d) PXRD patterns of ZIF-8 NCs before and after soaking in MeOH for 12 h. (e, f) TEM images of (e) pristine EZP-L and (f) soaked in MeOH for 12 h. (g) Edge length distribution histogram and (h) PXRD patterns of EZP-L before and after soaking in MeOH for 12 h.

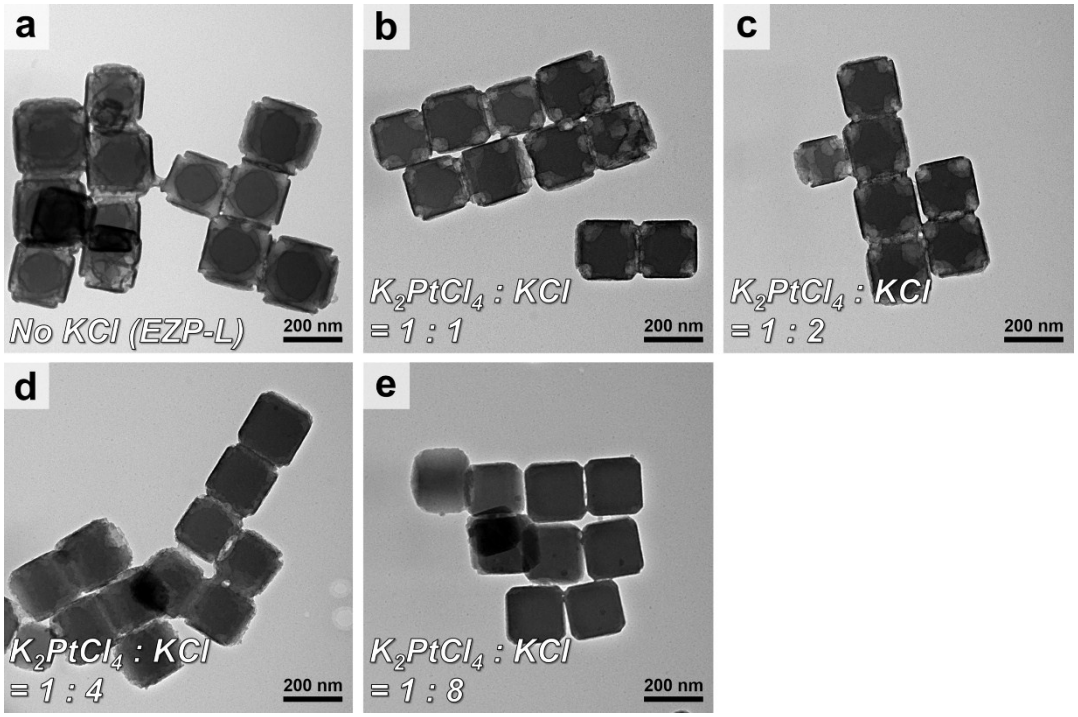

Figure S17. TEM images of EZP-L with added KCl; (a) without KCl, (b) 0.025 mmol, (c) 0.05 mmol, (d) 0.1 mmol and (e) 0.2 mmol of KCl. With increasing amount of KCl, the exchange of Pt^{2+} ions and corrosion of ZIF-8 were suppressed.

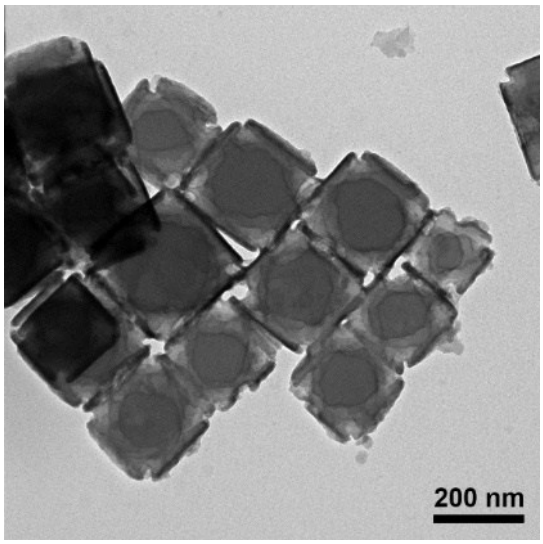

Figure S18. TEM image of EZP-L nanocrystals soaked for 12 h in MeOH in presence of KCl (0.1 mmol)

In the presence of chloride ions, the structure transformation of EZP-L did not occur even the EZP-L was soaked in MeOH for 12 h. Therefore, it seems that the reaction did not proceeded after 12 h (24 h, **Figure S10f**), because of free chloride ions in reaction media which are generated from K_2PtCl_4 precursor.

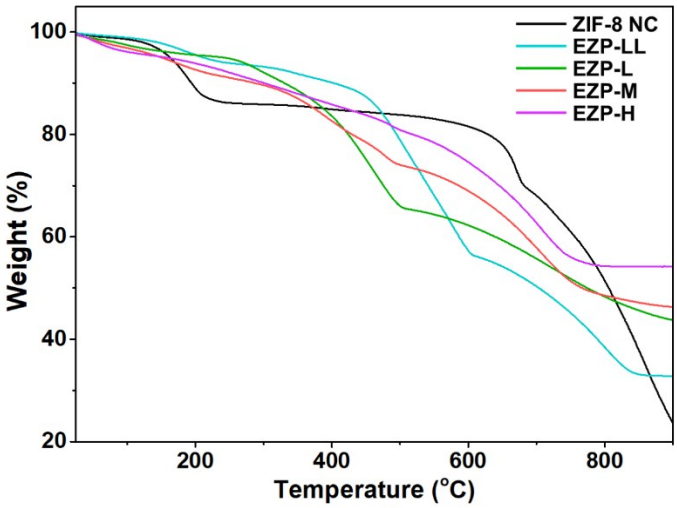

Figure S19. TGA curves of ZIF-8 NC, EZP-LL, EZP-L, EZP-M and EZP-H samples under N_2 atmosphere.

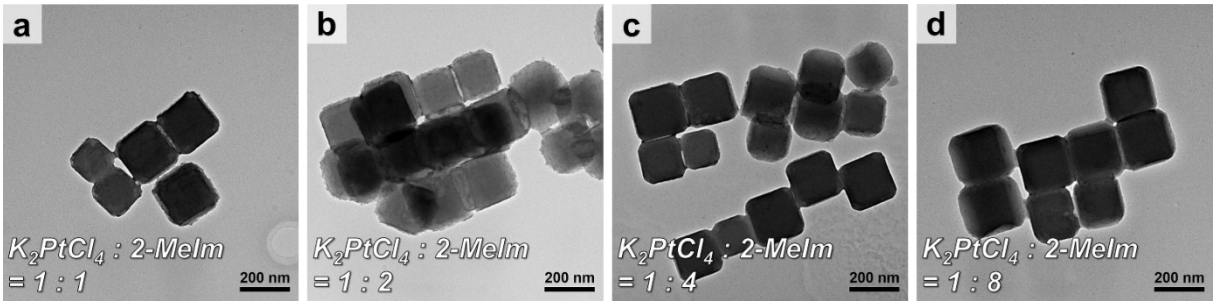

Figure S20. TEM images of EZP-L with added 2-MeIm; (a) 0.025 mmol, (b) 0.05 mmol, (c) 0.1 mmol and (d) 0.2 mmol of 2-MeIm. With increasing amount of 2-MeIm, the exchange of Pt^{2+} ions and corrosion of ZIF-8 were also suppressed.

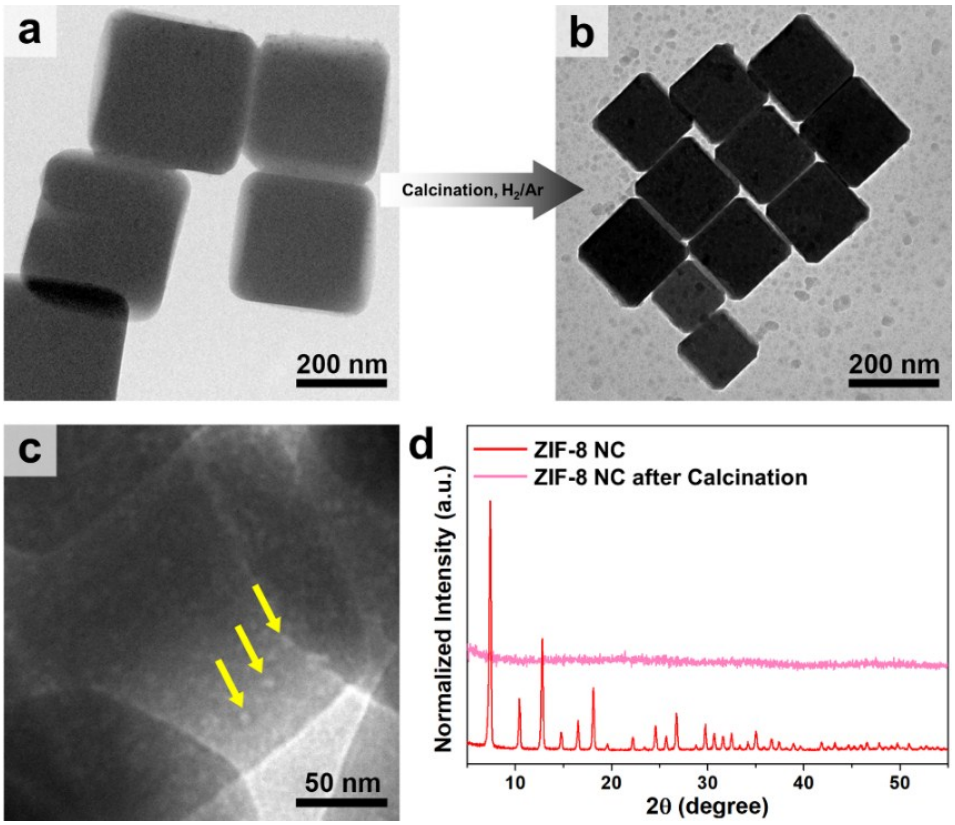

Figure S21. (a, b) TEM images of ZIF-8 NCs (a) before and (b) after calcination at 550 °C under H_2 (5%, Ar-balanced) condition. (c) Enlarged TEM image of ZIF-8 NCs after calcination. Yellow arrows indicate the pores in the calcined ZIF-8 NCs. (d) PXRD patterns of ZIF-8 NCs before and after calcination.

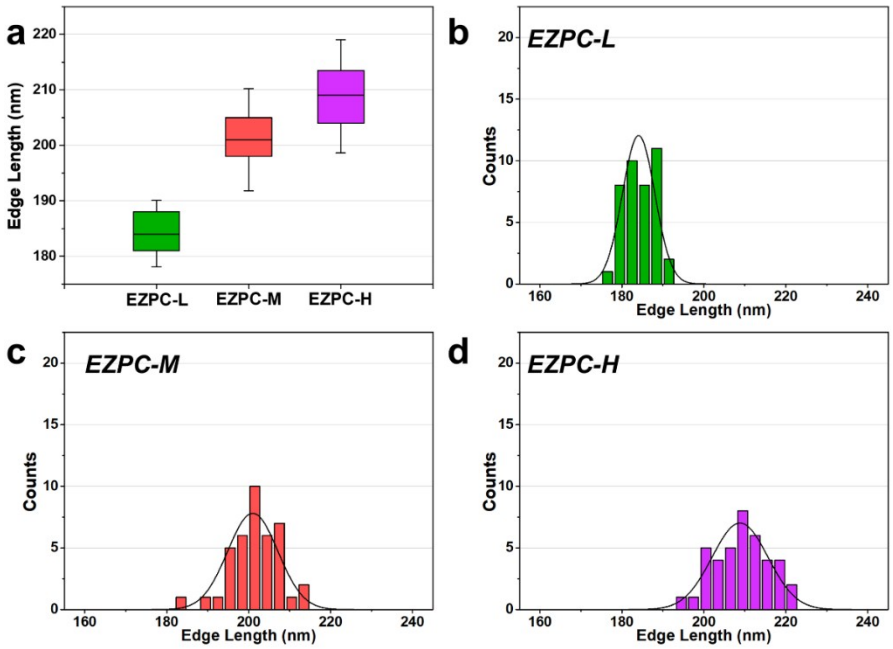

Figure S22. (a) Edge length distribution of EZPC-X (X = L, M and H) (b-d) Edge length distribution histogram of (b) EZPC-L, (c) EZPC-M and (d) EZPC-H.

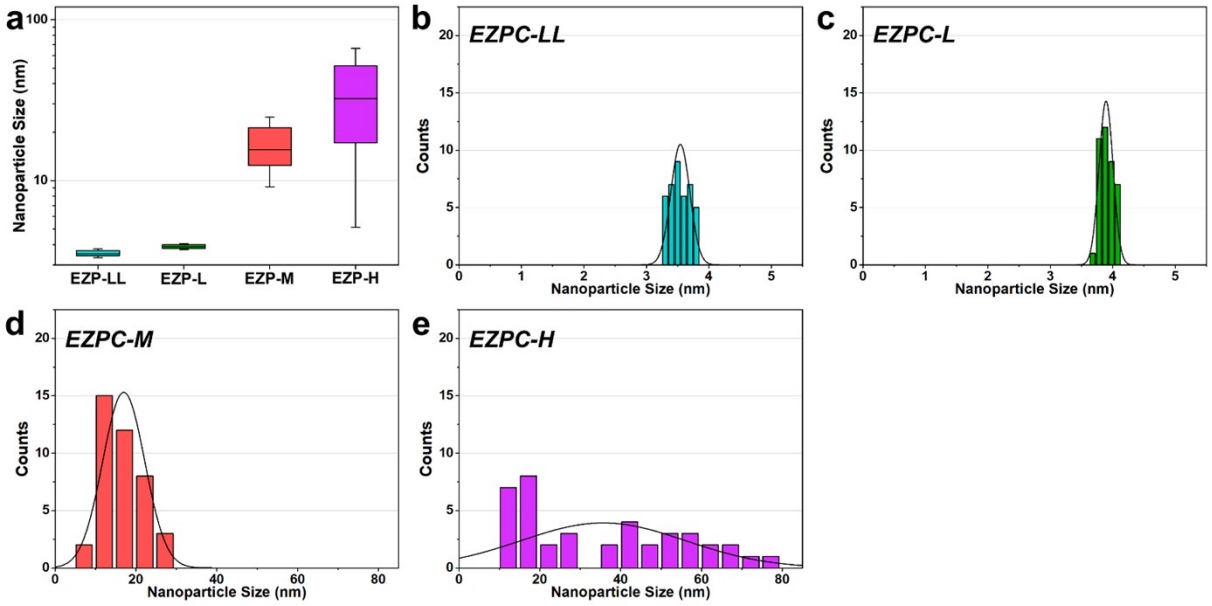

Figure S23. (a) Size distribution of embedded nanoparticles in EZPC-X (X = LL, L, M and H) (b-e) Size distribution histogram of embedded nanoparticles of (b) EZPC-LL, (c) EZPC-L, (d) EZPC-M and (e) EZPC-H.

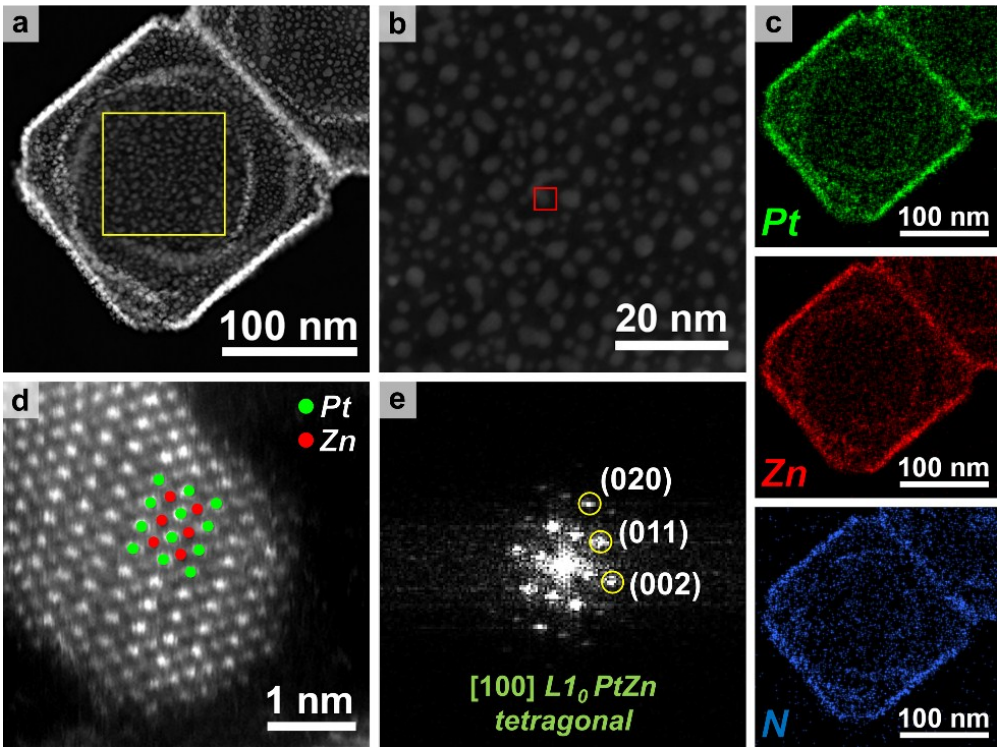

Figure S24. (a) HAADF-STEM image of EZPC-L. (b) Enlarged HAADF-STEM image of EZPC-L of the yellow box in Figure S17a. (c) Corresponding EDX elemental mapping analysis of Pt (green), Zn (red) and N (blue) content in EZPC-L shown in Figure S17a. (d) High resolution HAADF-STEM image in the red box in Figure S17b and (e) its corresponding FFT pattern of EZPC-L in the red box in Figure S17b. The red and green spheres represent Zn and Pt atoms.

The ordered structure is shown by alternating bright (Pt) and dark (Zn) contrast, whose zone axis was [100] **(Figure S24d and S24e)**. Also, the EDX elemental mapping analysis of EZPC-L revealed the homogeneously dispersed Pt and Zn content in the particle of EZPC-L **(Figure S24c)**. N content derived from N-doped carbon nanocage was also detected uniformly on overall EZPC-L structure.

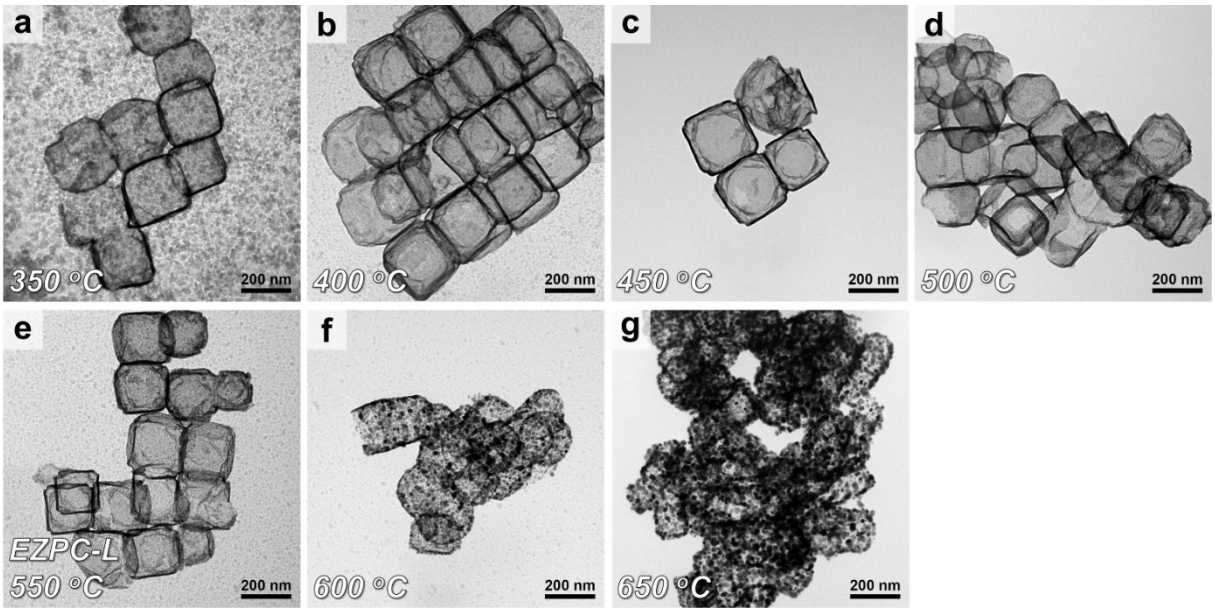

Figure S25. TEM images of calcined EZP-L samples with different temperature: (a) 350 °C, (b) 400 °C, (c) 450 °C, (d) 500 °C, (e) 550 °C (EZPC-L), (f) 600 °C and (g) 650 °C.

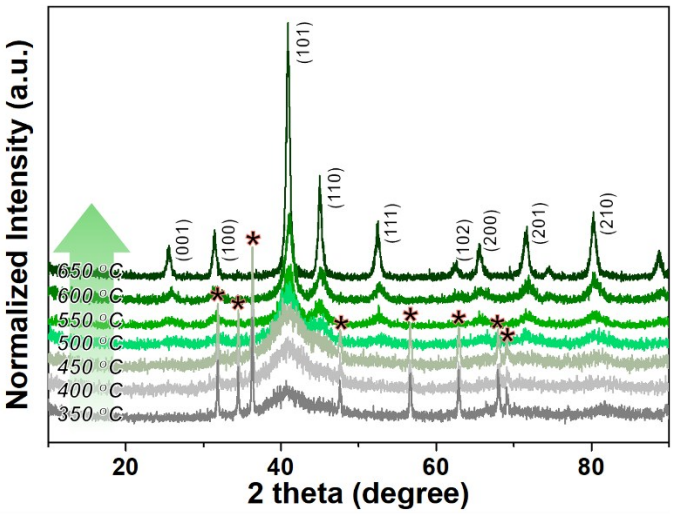

Figure S26. PXRD patterns of calcined EZP-L samples with different temperature. Asterisks in the graph indicates hexagonal ZnO phase (JCPDS #01-074-9939).

By PXRD patterns of calcined EZP-L samples with various temperature, the calcination temperature at 350 to 450 °C was required for the formation of A1-type PtZn random alloy nanoparticles **(Figure S26)**. The formation of ZnO phase was observed at lower temperature. The tetragonal $L1_0$-PtZn intermetallic phase was observed only when the calcination temperature was higher than 500 °C. However, when the calcination temperature was higher than 600 °C, the rupture of cubic nanocage structure was observed due to high thermal energy **(Figure S25f and S25g)**. The FWHM of PXRD pattern was decreased with increasing calcination temperature, due to the increase in size of embedded nanoparticles **(Figure S26)**.

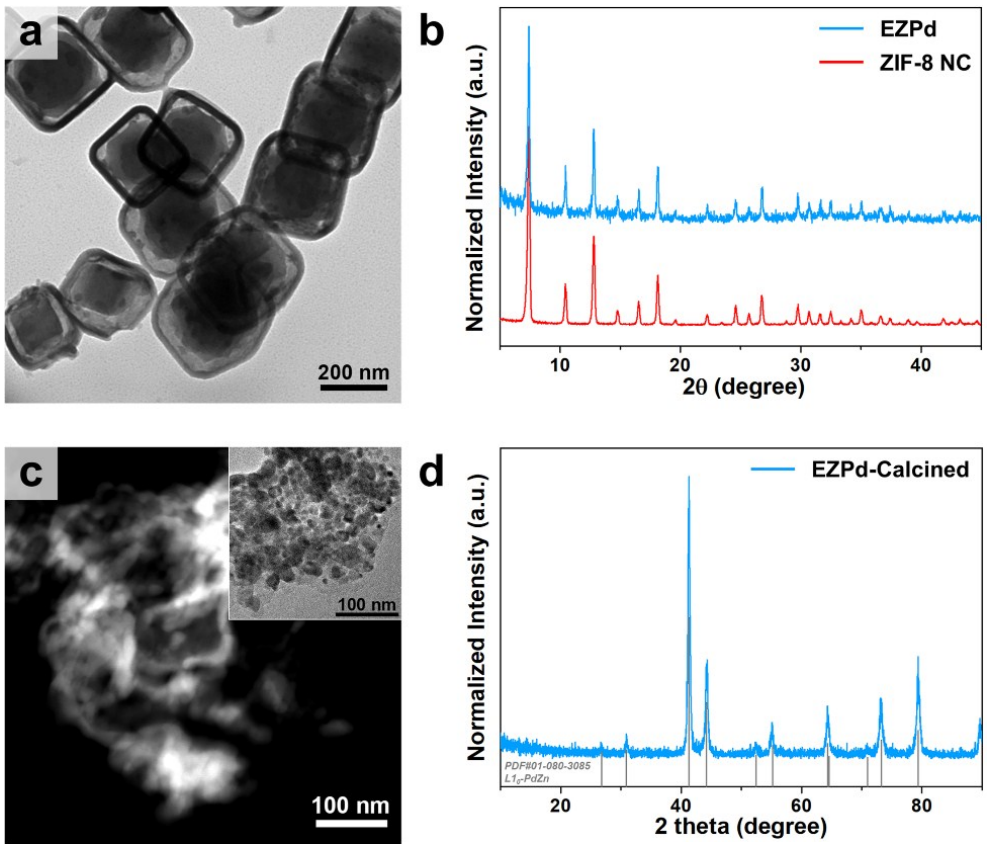

Figure S27. (a) TEM image of Pd^{2+}-exchanged ZIF-8 NCs (EZPd, K_2PdCl_4 as a precursor). (b) PXRD patterns of EZPd and ZIF-8 NC. (c-d) (c) HAADF-STEM image (inset: TEM image) and (d) PXRD pattern of calcined EZPd. Features of intermetallic $L1_0$-PdZn were observed after calcination.

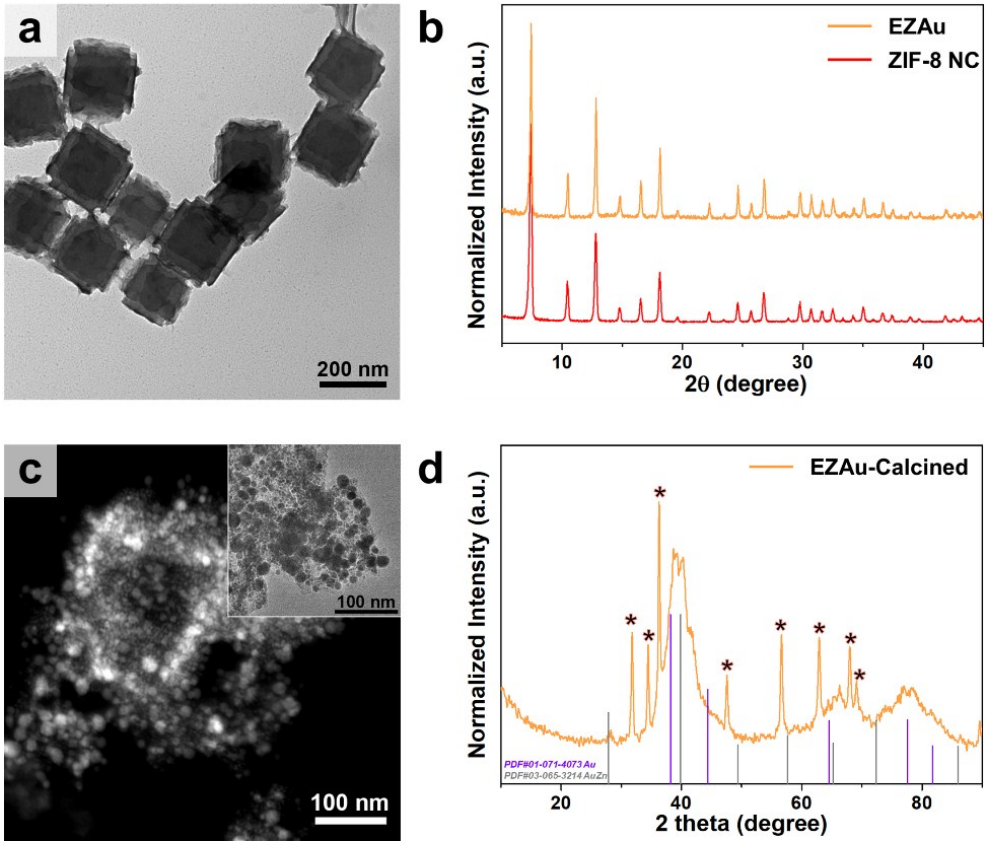

Figure S28. (a) TEM image of Au^{3+}-exchanged ZIF-8 NCs (EZAu, $KAuCl_4$ as a precursor). (b) PXRD patterns of EZAu and ZIF-8 NC. (c-d) (c) HAADF-STEM image (inset: TEM image) and (d) PXRD pattern of calcined EZAu. Asterisks in the graph indicate hexagonal ZnO phase (JCPDS #01-074-9939). Unlike Pt and Pd case, features of metallic Au and intermetallic AuZn were simultaneously observed.

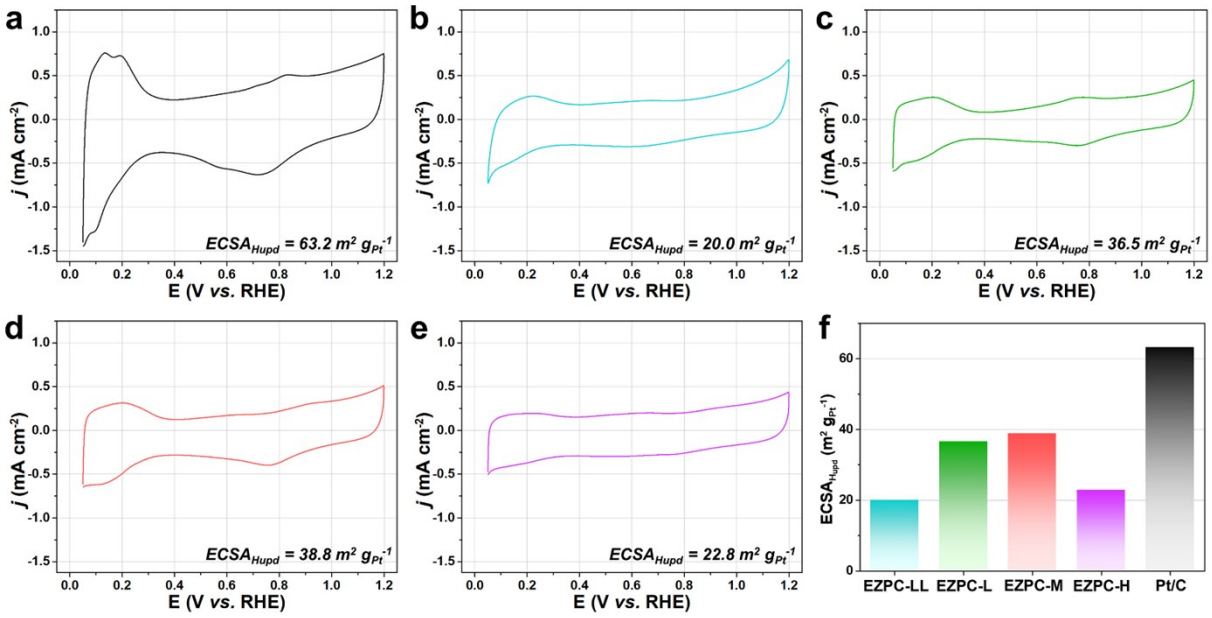

Figure S29. Cyclic voltammogram (CV) curves of (a) 10 wt% Pt/C, (b) EZPC-LL/C, (c) EZPC-L/C, (d) EZPC-M/C and (e) EZPC-H/C under N_2-saturated 0.1 M $HClO_4$ electrolyte. (f) Comparison of calculated $ECSA_{Hupd}$ values of the catalysts.

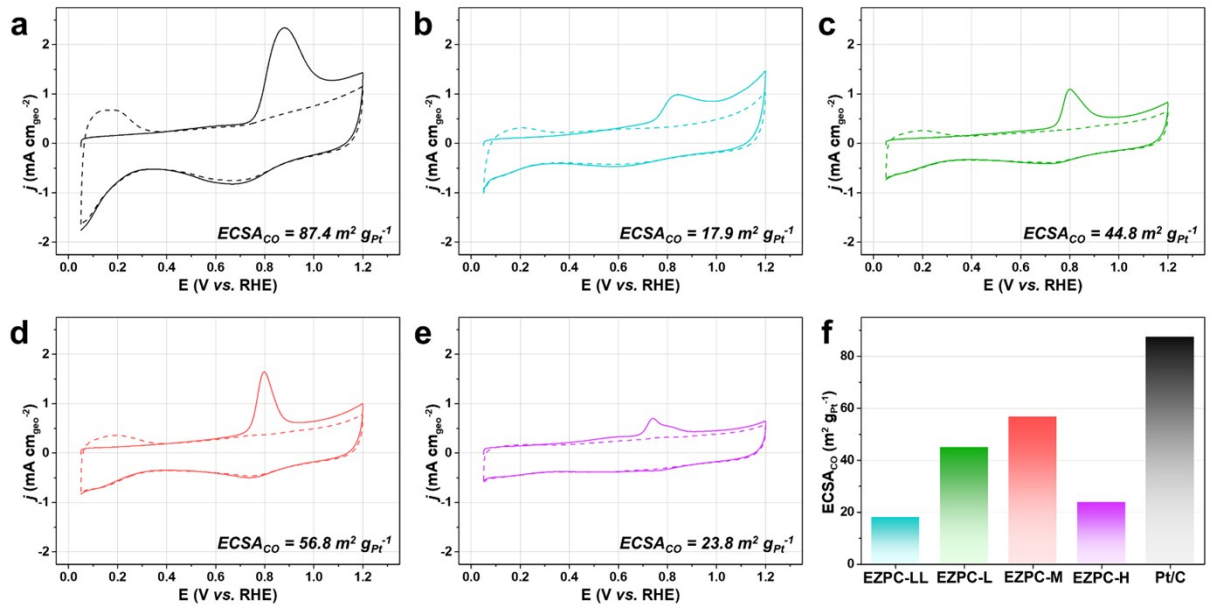

Figure S30. CO-stripping measurements of the catalysts. (a) 10 wt% Pt/C, (b) EZPC-LL/C, (c) EZPC-L/C, (d) EZPC-M/C and (e) EZPC-H/C. (f) Comparison of calculated $ECSA_{CO}$ values of the catalysts.

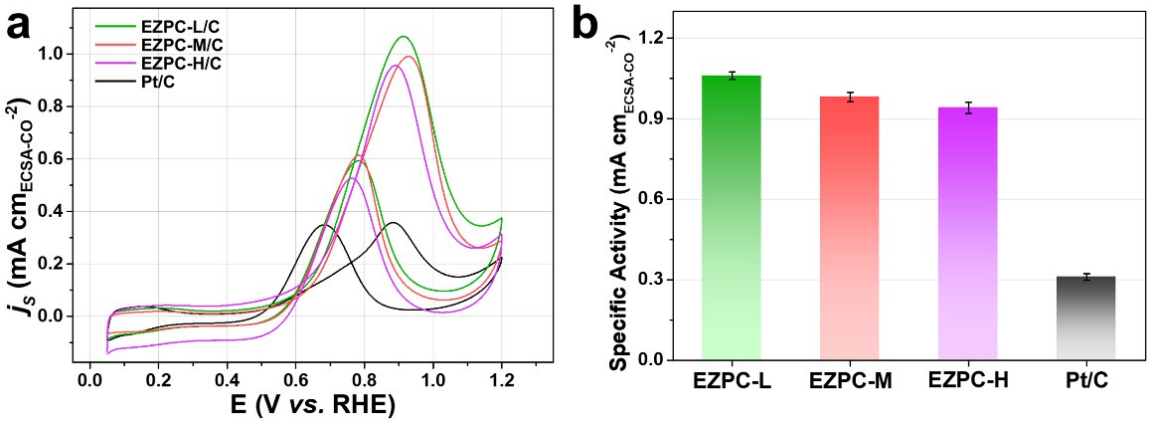

Figure S31. (a) MOR CV curves of the catalysts normalized by CO-stripping derived ECSA ($ECSA_{CO}$). (b) Comparison of MOR specific activities of the catalysts normalized by $ECSA_{CO}$.

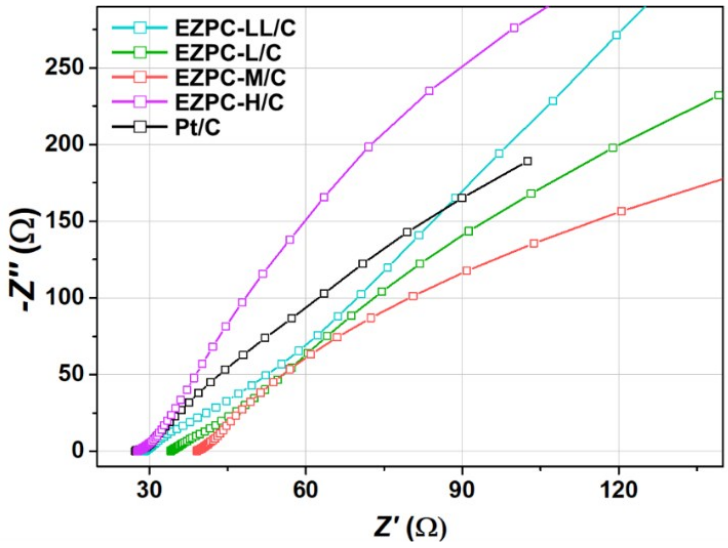

Figure S32. Electrochemical impedance spectroscopy (EIS) Nyquist plots in 0.1 M $HClO_4$ + 1.0 M MeOH electrolyte.

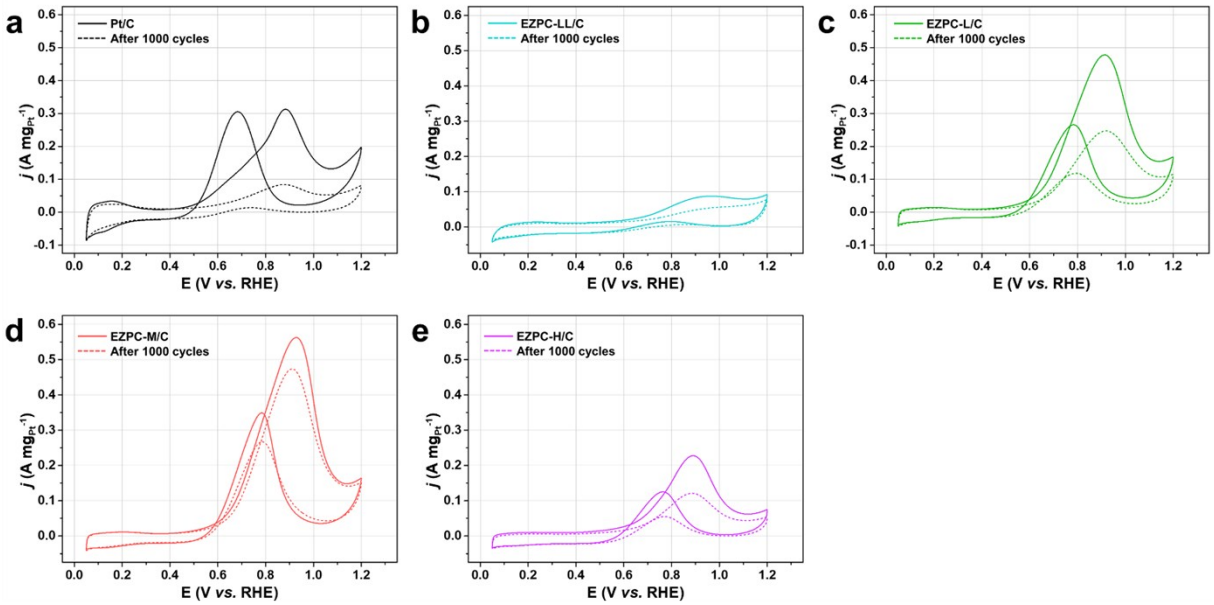

Figure S33. MOR CV curves of the catalysts before and after durability test with potential cycling between 0.4 and 0.9 V (*vs*. RHE) under N_2-saturated 0.1 M $HClO_4$ + 1.0 M MeOH electrolyte; (a) Pt/C, (b) EZPC-LL/C, (c) EZPC-L/C, (d) EZPC-M/C and (e) EZPC-H/C.

Reference

S1. C. Zhao, X. Dai, t. Yao, W. Chen, X. Wang, J. Wang, J. Yang, S. Wei, Y. Wu and Y. Li, *J. Am. Chem. Soc.*, 2017, **139**, 8078.